Research Article | Vol. 28, No. 19 / 14 September 2020 / Optics Express 27644
Optics EXPRESS

Self-powered broadband photo-detection and persistent energy generation with junction-free strained Bi_2Te_3 thin films

BRUNO LORENZI,[1,2,4] YOICHIRO TSURIMAKI,[1] AKIHIRO KOBAYASHI,[3] MASAYUKI TAKASHIRI,[3] AND SVETLANA V. BORISKINA[1,5]

[1]Department of Mechanical Engineering, Massachusetts Institute of Technology, Cambridge, MA 02139, USA
[2]Department of Materials Science, University of Milano Bicocca, Milan, Italy
[3]Department of Materials Science, Tokai University, Hiratsuka, Japan
[4]bruno.lorenzi@unimib.it
[5]sborisk@mit.edu

Abstract: We experimentally demonstrate efficient broadband self-powered photo-detection and power generation in thin films of polycrystalline bismuth telluride (Bi_2Te_3) semiconductors under inhomogeneous strain. The developed simple, junction-free, lightweight, and flexible photo-detectors are composed of a thin active layer and Ohmic contacts on a flexible plastic substrate, and can operate at room temperature and without application of an external bias voltage. We attribute the observed phenomena to the generation of an electric field due to a spontaneous polarization produced by strain gradient, which can separate both photo-generated and thermally-generated charge carriers in bulk of the semiconductor material, without a semiconductor junction. We show that the developed photo-detectors can generate electric power during both the daytime and the nighttime, by either harnessing solar and thermal radiation or by emitting thermal radiation into the cold sky. To the best of our knowledge, this is the first demonstration of the power generation in a simple junction-free device under negative illumination, which exhibits higher voltage than the previously used expensive commercial HgCdTe photo-diode. Significant improvements in the photo-detector performance are expected if the low-charge-mobility polycrystalline active layer is replaced with high-quality single-crystal material. The technology is not limited to Bi_2Te_3 as the active material, and offers many potential applications in night vision, wearable sensors, long-range LIDAR, and daytime/nighttime energy generation technologies.

1. Introduction

Infrared detectors and photon-to-electric-current energy converters usually rely on the use of either p-n or Schottky junctions to separate the non-equilibrium photo-generated carriers [1,2]. p-n junction formation is one of the most difficult fabrication steps for photo-detectors, as it requires additional processing of the devices, may consume a substantial amount of energy, and ultimately increases the time and cost of device fabrication. Most importantly, in all types of photo-detectors based on the charge carrier separation by a semiconductor junction, the photo-voltage does not exceed the electronic band gap of the material [3,4], which limits their responsivity. Furthermore, junction capacitance limits the speed of operation of all photo-diodes and amplifies shot noise caused by current flowing across a junction. While photo-diodes can be operated in a self-powered photovoltaic mode (i.e. without the external bias), they are typically reverse-biased to decrease junction capacitance, to increase responsivity, and to enable operation in the linear-response regime. Infrared photo-detectors typically also require cooling to reduce dark current and increase responsivity, further increasing the system cost and footprint.

#399040 https://doi.org/10.1364/OE.399040
Journal © 2020 Received 1 Jun 2020; revised 20 Aug 2020; accepted 20 Aug 2020; published 3 Sep 2020

Optics EXPRESS

Other types of infrared detectors make use of the photoconductive effect of reduced resistance caused by the photo-generated carriers [5,6]. These devices offer room temperature operation as well as higher detection capability and faster response speed than infrared p-n diodes based on other material systems. However, they require external bias for operation, and cannot be used in a self-powered mode, which limits their range of applications.

On the other hand, some materials exhibit 'bulk photovoltaic effect,' manifested as the spontaneous electrical polarization in the bulk of material, without any junction [7]. These materials are characterized by crystal lattices that belong to non-centrosymmetric space groups, and can exhibit built-in polarization either in response to an applied mechanical strain (piezoelectric materials) or as a result of spontaneous polarization alignment of atoms grouped in domains (ferroelectrics) [8,9]. The voltage induced due to such spontaneous polarization can exceed the electronic bandgap of the material by several orders of magnitude, offering intriguing opportunities for the photon energy harvesting beyond the SQ limit and efficient photo-detection [10]. However, the use of piezoelectric or ferroelectric materials to develop photovoltaic cells or photo-detectors has been limited, because most of them exhibit large electronic bandgaps, and thus cannot be used to detect infrared (or even most of the visible) light.

Fortunately, a flexo-electric effect (from Latin 'flexus' meaning 'bend') – a higher-order electromechanical effect that couples a spontaneous material polarization to a *gradient* of mechanical strain – is a universal phenomenon that can be observed not only in piezo- and ferroelectric materials but also (to some degree) in all dielectrics and semiconductors [9,11–13]. Previous studies of flexo-electricity in non-centrosymmetric materials revealed that ferroelectric transitions could be induced by applying strain to the thin films of ferroelectrics even at temperatures above their ferroelectric transition (Curie) temperature [14]. Furthermore, it has been shown that in strained piezoelectric materials, voltage output contributed by flexo-electric effect can exceed manifold that solely contributed by the piezoelectric effect [15].

Recently, flexo-electricity has been proposed as a novel approach to harvest energy from acoustic vibrations [9,15,16], heat gradients [17,18], and solar radiation [19]. Here, we demonstrate that strain gradients can be induced in narrow-bandgap semiconductors to develop room-temperature infrared photo-detectors, which can operate either in the self-powered regime for wearable technologies or in the biased regime for long-range light detection and ranging (LIDAR) and night vision applications. Simple, junction-free, and lightweight detector prototypes composed of thin semiconductor layers on flexible substrates have been fabricated, and exhibited photo-voltages and responsivities competitive with the state of the art junction-type photo-detectors when operated at room temperature and without application of an external bias. These junction-free devices can serve as broadband detectors from the ultraviolet to the mid-infrared spectral range.

Furthermore, we show here that the developed devices can generate electric power during both the daytime and the nighttime, by either harnessing solar radiation (i.e., in the 'positive-illumination' solar-cell-like regime) or by emitting thermal radiation into the cold sky (i.e., in the 'negative-illumination' thermoradiative cell regime [20–22]). To the best of our knowledge, this paper reports on the first-ever experimental observation of the generation of a photo-voltage in a junction-free low-cost device under the 'negative' illumination scenario, with the device facing either a lower-temperature surface or a nighttime sky.

2. Junction-free strained photo-detector concept and device prototypes

Figure 1(a) shows a schematic of a thin-film junction-free photo-detector, composed of a polycrystalline bismuth telluride (Bi_2Te_3) material layer deposited on a flexible polyimide substrate. The strain gradient is introduced in the device by uniaxial bending of the substrate. The bending deformation induces compressive strain at the bottom of the device, and tensile strain on the top, with a zero-strain (neutral) surface in between. The fabrication process may also generate some residual strain gradients in the semiconductor film (i.e., caused by crystal

Optics EXPRESS

dislocations or grain/domain boundaries and by the polyimide substrates shrinkage during the film deposition [23]) in addition to the externally-applied bending strain. The in-plane and out-of-plane components of the strain tensor in the active layer can be expressed as follows (see Section 5): $\varepsilon_x = \varepsilon_r + (z - z_0) \cdot {R_c}^{-1}$ and $\varepsilon_z = -\nu\varepsilon_x/(1-\nu)$, where z measures the distance across the device in the vertical direction from the bottom surface of the substrate, the neutral plane is at position z_0, ε_r characterizes the residual strain existing in the sample prior to bending, and $(z - z_0) \cdot {R_c}^{-1}$ defines the bending contribution, which depends linearly on the distance from the neutral plane and is inversely proportional to the radius of the bending curvature. ν is the Poisson's ratio. The bending-induced strain gradient in the film can then be easily controlled by varying the device curvature radius: $\delta\varepsilon = \partial\varepsilon_x/\partial z = {R_c}^{-1}$.

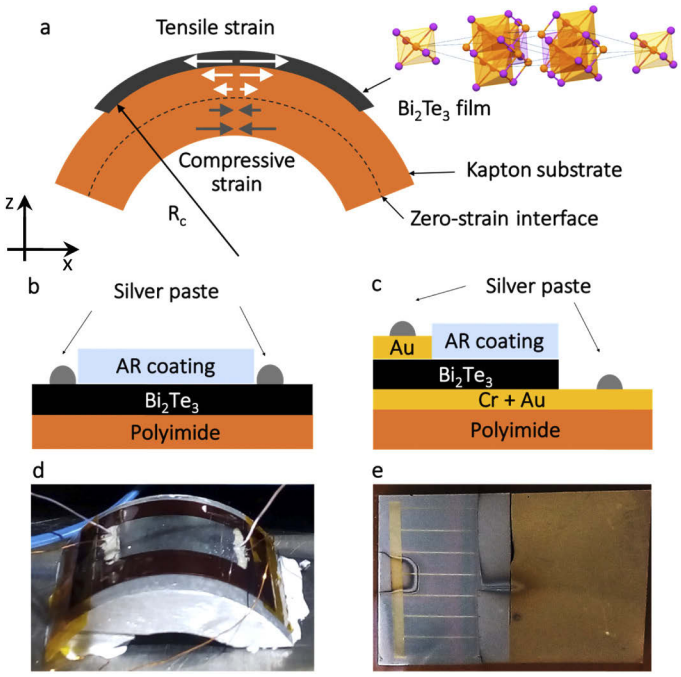

Fig. 1. Strained photo-detector device concept and prototypes. (a) A strained junction-free detector concept: a narrow-gap semiconductor thin film on a flexible substrate, with the strain gradient in the active layer formed by substrate bending. (b)-(c) Schematics of the fabricated detector prototypes comprising a polyimide substrate, a Bi_2Te_3 active layer, Ohmic metal contacts in either lateral (b) or vertical (c) configuration, and an anti-reflective (AR) Si_3N_4 coating layer. (d)-(e) Photographs of the fabricated lateral (d) and vertical (e) detector prototypes.

The strain gradient induced in the active layer results in the material polarization. In the general case of a non-ferroelectric material, the total internal polarization is a sum of the dielectric response to the applied electric field governed by the dielectric susceptibility tensor χ, the piezoelectric response to the homogeneous strain governed by the piezoelectric tensor $d = -\chi\lambda$, and the flexo-electric response to the strain gradient governed by the flexo-electric tensor $f = -\chi\mu$: $P_i = \chi_{ijk}E_{jk} + d_{ijk}\varepsilon_{jk} + f_{ijkl}\partial\varepsilon_{jk}/\partial x_l$ [9,11,13]. The first term in this formula disappears in the absence of the external driving field, and the bulk piezoelectric effect is forbidden by symmetry in the centrosymmetric material systems. Bending-induced strain gradient, however, creates built-in polarization in the bulk of a material with any lattice symmetry in its unstrained state. Furthermore, bending of a thin film can also induce polarization resulting from both

Optics EXPRESS

bulk piezoelectric and surface piezoelectric effects, the former caused by the bandgap variation induced by the asymmetry between the compressive strain on the concave surface and the tensile strain on the opposite-side convex surface, and the latter – by the lattice symmetry breaking at the surface [9,13,24–27]. In the polycrystalline films, symmetry breaking at the grain boundaries may introduce additional polarization under bending deformation. All these contributions can be lumped together to form an effective flexo-electric coefficient (typically defined as polarization divided by curvature) [13].

Bending deformation induces elastic strain in the device in both in-plane and out-of-plane directions, and the resulting strain-gradient-induced electric field in the active layer has both x- and z-components. Accordingly, separation of photo-generated charge carriers in the photo-detector can be achieved either in lateral (Fig. 1(b)) or in vertical (Fig. 1(c)) device architectures. To evaluate the performance of both architectures, we fabricated two types of photo-detector prototypes: (i) lateral detectors, with two Ohmic electrical contacts placed on the active layer top surface (Fig. 1(d)), and (ii) vertical detectors, with the two Ohmic contacts placed at the top and bottom surfaces of the active layer (Fig. 1(e)). In the former configuration, the photo-generated current driven by the internal electric field flows laterally in the plane on the device, while in the latter it flows in the vertical direction across the active layer thickness.

The bismuth telluride thin films were deposited by either DC (Fig. 1(d)) or RF magnetron (Fig. 1(e)) sputtering at a substrate temperature of 200°C. To improve the light absorptance properties of the fabricated devices, they were covered with silicon nitride (Si_3N_4) anti-reflection layers with the thickness of 800 nm. Deposition of a quarter-wavelength-thick Si_3N_4 layer nearly doubled the average absorptance of the broadband solar radiation in the photo-detectors

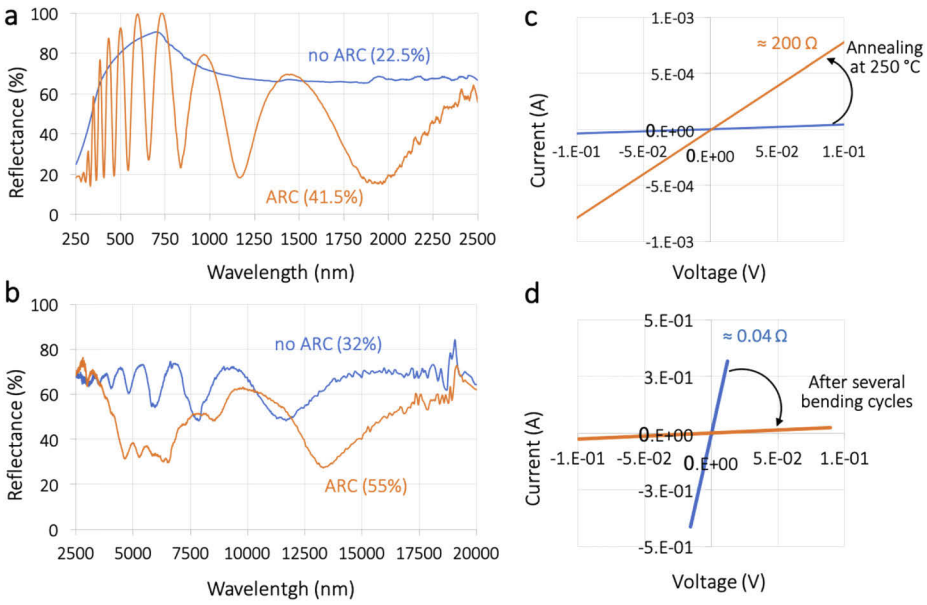

Fig. 2. Photo-detector material properties can be improved via annealing and anti-reflective coating deposition and degrade after multiple bending cycles. (a)-(b) Measured visible-to-mid-infrared light reflectance spectra of the 1.6 micron-thick polycrystalline Bi_2Te_3 film on a polyimide substrate with (orange lines) and without (blue lines) Si_3N_4 ARC layers of 800 nm in thickness. The labels correspond to the illumination-spectrum-weighted absorptance of the samples. (c)-(d) The I-V curves of both lateral (c) and vertical (d) devices exhibit linear behavior, with resistance decreasing after annealing (c) and increasing as a result of bending-induced deformations (d).

Optics EXPRESS

(e.g., the solar-spectrum-weighted absorptance in the visible and near-infrared spectral range increased from 22.5% to 41.5% for the sample in Fig. 1(d)), as shown in Fig. 2(a). Likewise, the near-to-mid-infrared absorptance of the detector weighted to the blackbody radiation spectrum at 500K (Fig. 2(b)) has been increased to 55% by the ant-reflective coating (ARC) deposition. Note that absorptance exceeds 80% at select wavelengths and can be further optimized by better ARC designs.

Either gold (Au) and silver (Ag) Ohmic contacts have been demonstrated to provide electrical performance of the fabricated devices with linear current-voltage (I-V) characteristics, with the slope of the I-V curve providing a measure of the electrical resistance of each device (see Figs. 2(c) and 2(d)). To improve their material properties, the samples were annealed in vacuum for two hours at 250°C, which resulted in the significant decrease of the device resistance (see Fig. 2(c)). However, after the prototypes have been subjected to several bending deformations, some degradation in the device performance has been observed (Fig. 2(d)), likely associated with defects developed in either the active layer or the Ohmic contacts. After initial degradation, the resistance stabilized and did not vary during the bending cycles in the process of the device performance characterization.

It should be noted that in a practical realization of the proposed photo-detectors, the material would not be subjected to multiple bending cycles that degrade its electronic performance. The active material layer deposited on a flexible substrate will either be bent only once or will be fabricated on a pre-strained substrate, which will be subsequently flattened to induce the strain gradient [23]. The *in-situ* strain can also be induced by either using textured substrates or by covering the active material with over-layers with engineered stress/strain gradients [28–31]. Such *in-situ* strain generation makes possible fabrication of complementary metal–oxide–semiconductor (CMOS)-compatible flexoelectric photo-detectors and detector arrays.

3. Characterization of photo-detectors under illumination by artificial sunlight

The electrical performance of the fabricated devices has been tested under broadband illumination by the artificial sunlight (Fig. 3(a), see Section 5). The increasing level of strain gradient was introduced to the samples by progressively reducing the distance between the opposite sides of the substrate to bend the films (Fig. 3(a)). All the laboratory measurements have been performed inside a vacuum chamber to eliminate the effects of air convection, and the temperature of the sample has been monitored via attached thermocouples.

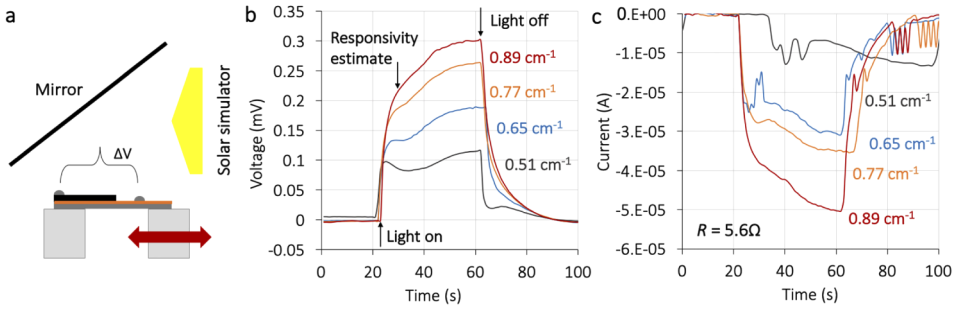

Fig. 3. Vertical photo-detector characterization under 'positive' illumination by artificial sunlight. (a) Schematic of the measurement setup. (b) Photo-voltage and (c) photocurrent measured under one-sun illumination and varying strain gradient. The labels correspond to the strain gradient values, and the initial fast slope of the signal rise has been used to calculate the device responsivity. The measured resistance of the photo-detector device is 5.6 Ω.

Optics EXPRESS

The photo-voltage and photocurrent measured in a vertical detector prototype under one-sun solar illumination are plotted in Figs. 3(b) and 3(c), and shown to increase with the increased strain gradient imposed on the sample (the strain gradient values are shown as labels on the plots). Both, voltage and current exhibit a sharp rise upon exposure to sunlight, followed by a slower increase on a longer timescale. We attribute the initial fast rise of the photo-signal to the separation of the photo-generated charge carriers by the internal field formed in the bent samples as a result of a combined action of the flexo-electric and piezoelectric effects induced by the strain gradient. This initial signal rise has been used below to calculate the device responsivity.

The slow component of the photo-signal rise is attributed to an additional current being generated via the thermoelectric effect in the active Bi_2Te_3 layer as it is heated due to absorptance of the incident sunlight under the continuous illumination [18,23]. Bi_2Te_3 is a well-known thermoelectric material, which exhibits electrical current driven by the Seebeck effect under thermal gradient in the material. When the light is turned off, a sharp signal decay is observed in Figs. 3(b) and 3(c), resulting from the fast material depletion of photo-generated free charge carriers upon their migration to the Ohmic contacts, followed by a slower decay likely caused by the material gradual cooling and the migration of trap-released charge carriers [32]. Both the photocurrent and the photo-voltage scale linearly with either the incoming photon power flux or the strain gradient (Figs. 4(a)–4(d)).

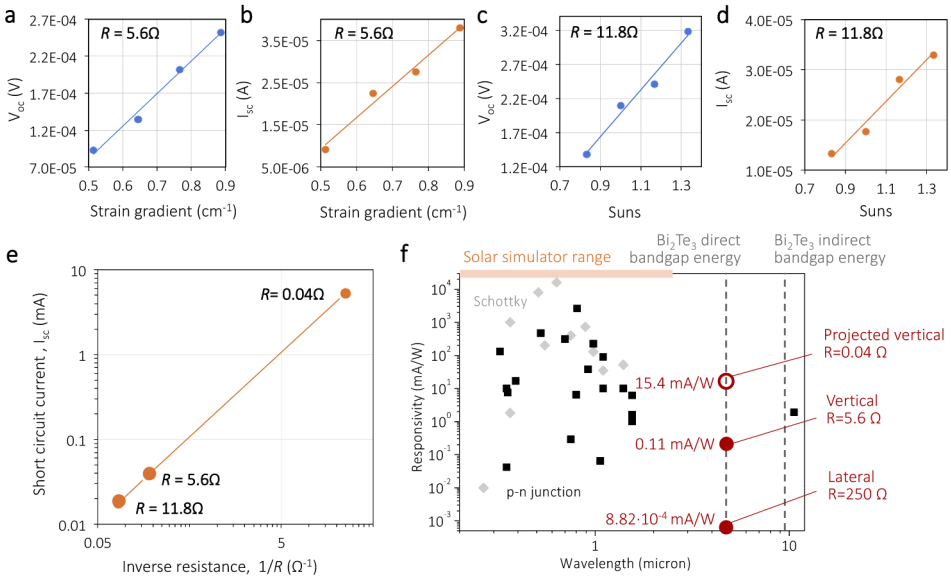

Fig. 4. Photocurrent and photo-voltage scale linearly with the strain gradient and incoming power, while photo-current also scales linearly with the inverse resistance. (a)-(b) Photo-voltage and photocurrent in a vertical detector with resistance of 5.6 Ω as a function of the strain gradient under one sun illumination. Experimental error (estimated as the standard deviation computed for the data from multiple measurements) for the strain gradient is ~10%, and for V_{oc} is ~3%. (c)-(d) Photo-voltage and photocurrent in a vertical detector with resistance of 11.8 Ω and strain gradient of 0.89 cm^{-1} as a function of the incident solar power. (e) Photocurrent scales linearly with the inverse resistance of the detector. (f) Responsivity of the lateral and vertical photo-detector prototypes under solar illumination compared to the responsivity values previously reported for different types of junction-based detectors operated in the self-powered regime.

Lateral detector prototypes exhibited similar behavior under illumination, but with significantly smaller photocurrents due to the high internal resistance of 250 Ω (Fig. 2(c)) in the centimeter-long

Optics EXPRESS

devices. Improvement of the internal resistance to 0.04 Ω (Fig. 2(d)), achieved by reducing the contact spacing from 2 cm in the lateral configuration to 1.5 micron in the vertical configuration increased the photocurrent output by several orders of magnitude. For example, the maximum photo-voltages measured in the self-powered lateral and vertical photo-detector prototypes under maximum strain gradient and one sun illumination had comparable values of 3.1×10^{-4} V and 2.6×10^{-4} V, respectively. However, due to the large difference in the internal resistance of the two configurations, the corresponding photocurrents would differ by four orders in magnitude.

Likewise, the increased resistance of the vertical prototypes led to the corresponding decrease in the measured photocurrent, which scales linearly with the inverse of the resistance (see Fig. 4(e)). We calculated the current responsivity of the photo-detectors as the ratio of the photocurrent to the total power of the incident radiation: $R_A = I_{ph}/P_{inc}$ $[A/W]$. The measured resposivities of the vertical and lateral devices with the strain gradient of 0.89cm^{-1} under artificial solar illumination with the total power equal to the power of one sun and without applied bias are plotted in Fig. 4(f). Figure 4(f) also provides comparison of these data to the corresponding values of the self-powered junction-type photo-detectors previously reported in the literature [33]. It can be seen that there is a lack of literature data for self-powered infrared photo-detectors, because they are typically operated under bias voltage and/or at cryogenic temperatures. The devices developed and investigated in this study help to fill this gap.

The measured responsivity value in a vertical photo-detector reported in Fig. 4(f) illustrates the feasibility of the proposed simple device to provide a competitive platform for self-powered infrared signal detection. It should be noted that our measurements have been performed under broadband illumination, while the detector responsivity value typically increases with wavelength and peaks at a frequency close to the material bandgap [34–36]. As such, the responsivity values reported for our devices provide the low-level estimate of the responsivity potentially achievable under laser illumination at a wavelength close to the Bi_2Te_3 bandgap. Although we did not measure the photocurrent in the strained vertical device under 1 sun illumination before its resistance degraded from 0.04 Ω to 5.6 Ω as the result of repeated bending, the linearity of the current scaling with the inverse resistance and the measured photo-voltage characteristics enable us to predict the possibility of achieving a high responsivity value above 15mA/W in a polycrystalline Bi_2Te_3 film with low charge carrier mobility of 10-50 $\text{cm}^2\text{V}^{-1}\text{S}^{-1}$ [23] under modest strain gradient of 0.89 cm^{-1} (see Fig. 4(f)). For comparison, charge carrier mobility in single-crystalline Bi_2Te_3 exceeds 500 $\text{cm}^2\text{V}^{-1}\text{S}^{-1}$ [37], which should translate into the corresponding improvement in the photocurrent.

4. Device characterization under radiative heat and 'negative' illumination

Next, we evaluated the feasibility of using junction-free strained photo-detectors for thermal imaging and energy generation from harvesting radiative heat or using the coldness of the universe as a radiative heat sink [20–22]. The vertical device performance was tested under the condition when it was facing a blackbody plate with temperature either higher or lower than that of the photo-detector (Fig. 5(a)). The former situation corresponds to the conventional 'positive' illumination regime, with the energy flux directed towards the photo-detector (Fig. 5(b)), while the latter corresponds to the 'negative' illumination regime, characterized by the reversed energy flux due to the reversed temperature gradient between the detector and the radiative environment (Fig. 5(c)) [2,38]. The two illumination conditions are illustrated in Figs. 5(b) and 5(c), and offer a way to use the photo-detector to harvest electromagnetic and thermal energy from the environment both in the daytime and in the nighttime. The energy that can be harvested includes solar radiation as well as waste heat from industry or residential buildings.

Energy generation under the 'negative' illumination condition in thermoradiative cells has recently been proposed theoretically [20,21] and demonstrated experimentally with a commercial HgCdTe photo-diode [22]. Our measurements shown in Fig. 5(d) illustrate that under both positive

Optics EXPRESS

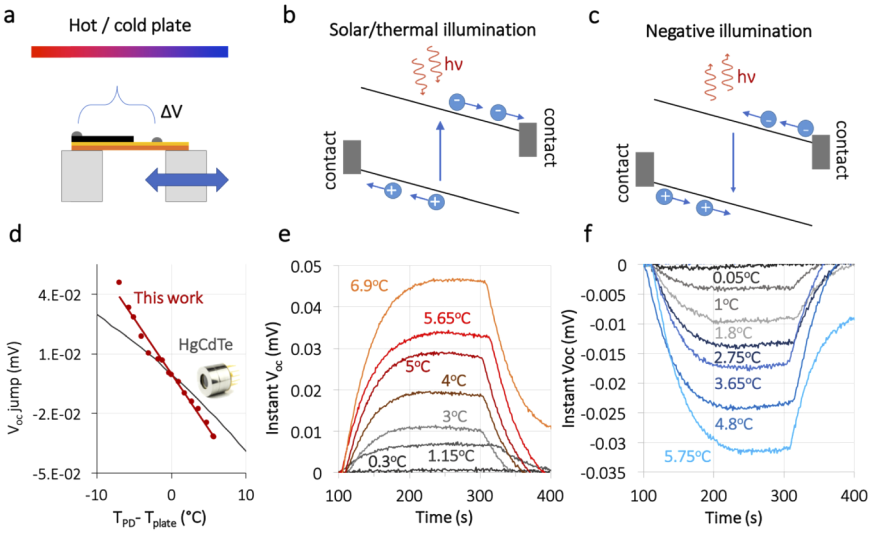

Fig. 5. Vertical photo-detector characterization under 'positive' and 'negative' thermal illumination. (a) Schematic of a measurement setup, with a vertical detector with a strain gradient of 0.5 cm^{-1} and resistance of 3.8 Ω facing a temperature-controlled plate. (b)-(c) Schematics illustrating the light absorption/emission process and the formation of the photocurrent in the device under 'positive' (b) and 'negative' (c) radiation conditions. (d) Measured photo-voltage in the detector as a function of the temperature gradient between the detector and the plate (red dots). Gray line shows the corresponding data previously reported for a commercial HgCdTe photo-detector under similar experimental conditions [22]. (e)-(f) The transient photo-voltage data recorded in the detector under positive (e) and negative (f) illumination and increasing temperature gradient (shown as labels on the plots).

and negative illumination conditions, higher voltage has been generated in a junction-free vertical photo-detector structure than previously reported when using a highly expensive commercial photo-diode based on a single-crystalline HgCdTe active layer. The transient photo-voltage data shown in Figs. 5(e) and 5(f) illustrate generation of the photo-voltage of different polarity under positive and negative illumination conditions, as expected. The photo-voltage increases with increase of the temperature gradient between the photo-detector and the radiative environment (represented by the hot/cold plate in this experiment). The data in Fig. 5 illustrates the possibility of using the junction-free strained photo-detectors for thermal imaging, remote temperature monitoring, and round the clock energy harvesting from the environment.

Finally, to test the device performance in realistic outdoors operation conditions, we repeated the negative illumination photo-detection test outdoors, with the vertical photo-detector prototype facing the night sky. The device was positioned within an enclosure facing upward as shown in Fig. 6(a) and covered by a Si wafer to reduce convective energy exchange with the environment. The test was conducted in Milan, Italy on January 19, 2020, and the photo-voltage of the same polarity as in the negative-illumination laboratory test has been recorded (Fig. 6(b)), demonstrating the feasibility of using junction-free flexoelectric detectors to harvest energy from the night sky while operating in the thermoradiative regime. It should be noted that the device performance can be further improved by using convection shields more transparent than Si (T~55%) in the mid-infrared spectral range, such as ZnSe (T>70%), polyethylene (T>90%), or a Si wafer with anti-reflective coatings, and by increasing the temperature gradient between the sky and the photo-detector. The optimum operation conditions depend on the balance between the

Optics EXPRESS

temperature-dependent radiative and non-radiative recombination rates in the active material [21], and will require further studies.

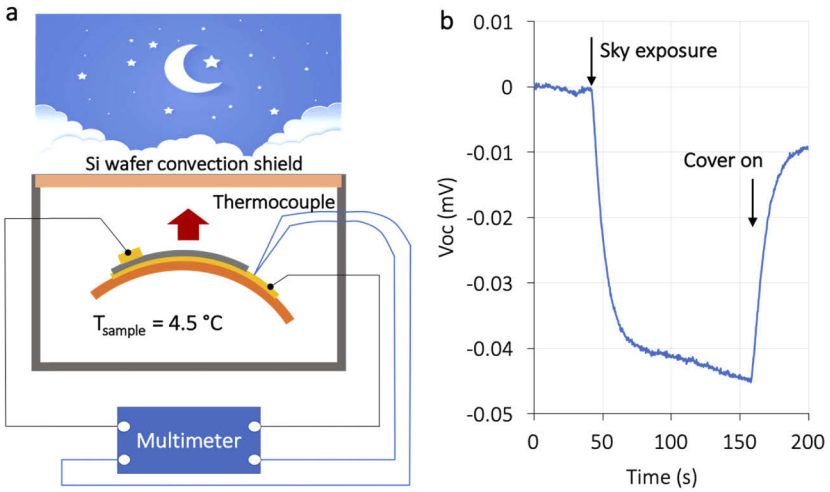

Fig. 6. Vertical photo-detector characterization under the 'negative' illumination from open sky at nighttime. (a) Schematic of a measurement setup, with a vertical detector with a strain gradient of 0.5 cm^{-1} and resistance of 3.8 Ω facing the sky and positioned inside a covered enclosure with a semi-transparent Si cover acting as the convection shield. (b) The transient photo-voltage data recorded in the detector shown in panel (a).

5. Methods

5.1. Device fabrication and characterization

The bismuth telluride thin films were deposited on flexible polyimide substrates by either DC or RF magnetron sputtering at a substrate temperature of 200°C [23]. To improve the light absorptance properties of the photo-detectors, some of the fabricated devices were covered with silicon nitride (Si_3N_4) anti-reflection layers with the thickness of 800 nm. The coating was deposited by the plasma-enhanced chemical vapor deposition (PECVD), and the ARC layer thickness was optimized to achieve efficient photon absorption at frequencies just above the bulk electronic bandgap of bismuth telluride. The weighted light absorptance of the samples for a specific light source (e.g., a solar simulator or a blackbody) within a given spectral range, has been calculated as follows. First, the sample reflectance (hereafter R) was measured for the given spectral range by means of an UV-Vis or an IR spectrometer. Then the ratio between the integral of the given source spectrum, and the integral of the same spectrum multiplied by (1-R) has been calculated.

Experimentally, solar illumination was achieved by using a Class AAA solar simulator (ScienceTech, SS-1.6 K) with a beam-down mirror to direct the artificial sunlight to the detectors. To simulate the one-sun illumination condition, the solar simulator was calibrated to output a radiative flux of 1000 Wm^{-2}. The photo-detector temperature was monitored in real time by a type K thermocouple and a multi-channel 2700 Keithley multimeter. The thermocouple was attached to the sample back contact and always covered with a piece of reflective tape, in order to keep it in dark, even when the sample was illuminated. The surface of the hot/cold plate facing the photo-detector was covered by an Acktar Light Absorbent Foil with a Metal Velvet coating (Edmund Optics), which provides over 97% absorptance/emittance in the mid-infrared spectral

Optics EXPRESS

range. The photo-generated voltage was measured by the same 2700 multimeter used for the temperature measurement, while the current was measured with a 2400 Keithley source meter.

The outdoors measurements of the detector performance under negative illumination were conducted at 1am local time in Milan, Italy on January 19, 2020. The ambient temperature during the measurement was about 2°C, and the local area humidity was around 80 percent.

5.2. Material properties characterization

The surface morphology of the deposited polycrystalline Bi_2Te_3 thin films was mapped by scanning electron microscopy (SEM: S-4800, Hitachi). A typical SEM image of the deposited thin films shown in Fig. 7(a) reveals the polycrystalline nature of the material.

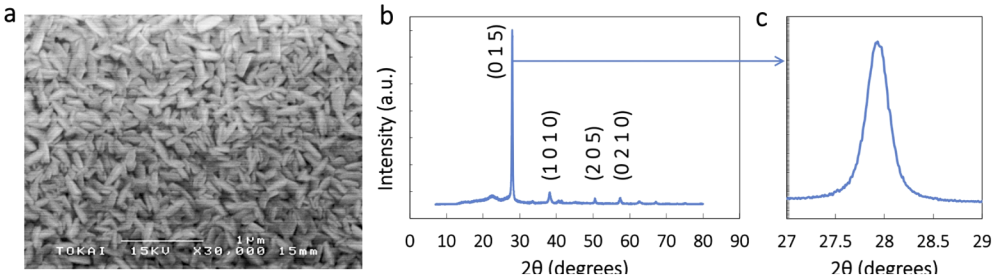

Fig. 7. Morphology of the polycrystalline Bi_2Te_3 thin films. (a) SEM image of a Bi_2Te_3 thin film deposited on a polyimide substrate. (b) XRD spectrum of the Bi_2Te_3 thin film. (c) The (0 1 5) XRD peak shown at higher resolution, whose FWHM was used to calculate an average crystallite size.

The crystallographic properties and lattice parameters of the films were determined by X-ray diffraction (XRD: Mini Flex II, Rigaku, CuKα radiation) at room temperature (Fig. 7(b)). All of the peaks in the XRD spectrum shown in Fig. 7(b) have been indexed to the rhombohedral phase of Bi_2Te_3 (JCPDS 33-0214). We found the average crystallite size to be around 30 nm, based on the estimates from the XRD peak broadening by using the Scherrer equation [39,40]: $L = K\lambda/Bcos\theta$. Here, L is the crystallite size, $B(2\theta)$ is the width of the (0 1 5) diffraction peak, in radians, at a height half-way between background and the peak maximum (full width at half maximum, FWHM), λ is the wavelength of the X-ray radiation (CuKaα $\lambda = 0.15418$ nm) and K is the Schrerrer constant (shape factor), usually taken as 0.89. The 30 nm average crystallite size is in agreement with prior literature data on the polycrystalline Bi_2Te_3 materials [23,41]. Furthermore, our prior work demonstrated that film bending in the opposite directions causes the opposite-sign spectral shift of the XRD peaks, providing a clear spectral signature of the bending-induced material strain [23].

The in-plane electrical conductivity of the annealed samples was measured at room temperature using a four-point probe method (RT-70 V, Napson), and ranged between $\sigma = 45\ S/\text{cm}$ and $\sigma = 78\ S/\text{cm}$ for different samples. The charge carrier concentration has been found to be $N = 1 \cdot 10^{19}\ \text{cm}^{-3}$ by the Hall effect measurements performed using the van derPauw method (HM-055, Ecopia). These data allowed us to estimate the charge carrier mobility in the annealed samples ranging from about $\mu = 28\ \text{cm}^2V^{-1}s^{-1}$ to $\mu = 48\ \text{cm}^2V^{-1}s^{-1}$. For comparison, our prior data measured on as-deposited polycrystalline Bi_2Te_3 thin films yielded mobility estimates on the order of $\mu = 10\ \text{cm}^2V^{-1}s^{-1}$ [23].

5.3. Strain engineering in flexible devices by bending deformations

In a flexible multi-layer stack under a uniaxial bending deformation, the in-plane elastic strain at any position z within the stack can be calculated as a product of the distance from this point to

Optics EXPRESS

the neutral plane and the film curvature: $\varepsilon_x = (z - z_0) \cdot K$ [28,42]. In a single-layer film with thickness d, the neutral plane characterized by zero stress and strain is located at the center of the film ($\varepsilon(z_n) = 0,\ z_n = d/2$). In the multilayer stack composed of several planar thin films deposited on a flexible substrate (Figs. 1(a)–1(c)), the differences between the elastic moduli of the individual films and the substrate cause the shift of the neutral plane from the mid-stack position. For the multilayer stack of total thickness $d = \sum_i d_i$, which is composed of m films with thicknesses d_i and the Young's moduli Y_i ($i = 1, \ldots m$), the position of the neutral plane can be calculated as: $z_0 = \frac{d}{2} - \frac{1}{2}\sum_i(Y_i \cdot \gamma_i \cdot d_i)/\sum_i(Y_i \cdot d_i)$, where $\gamma_i = \sum_j(\beta_{ij} \cdot d_j)$, and $\beta_{ij} = -1$ for $j \langle i; 0$ for $j = i$; and 1 for $j\rangle\, i$ [28,42,43]. The z-component of the elastic strain tensor direction is related to the in-plane x-component as $\varepsilon_z = -\nu\varepsilon_x/(1 - \nu)$, where ν is the Poisson's ratio of the film material.

Regardless the differences in the Young's moduli of different materials, the strain gradient along the vertical direction in the active semiconductor layer is inversely proportional to the radius of the sample curvature: $\partial\varepsilon_z/\partial z = (\varepsilon_z(z) - \varepsilon_z(z_0))/(z - z_0) = -\nu/(1 - \nu)R^{-1}$, $(R = K^{-1})$, which has been measured from the side photographs of the bent structures. The geometrical and mechanical parameters of all the materials used in the detector prototypes are summarized in Table 1 below [44,45].

Table 1. Mechanical parameters of the materials used in photo-detector structure.

Material	Thickness (μm)	Young's modulus (GPa)	Poisson's ratio
Bi_2Te_3	1.5	50 - 55	0.25
Polyimide	127	2.5 - 4	0.34
Si_3N_4	0.8	150-297	0.25
Au	0.1	79	0.42

6. Discussion and outlook

We demonstrated photo-detection and energy generation in narrow-bandgap semiconductor thin films subjected to inhomogeneous strain in the absence of semiconductor junction, and without external bias. We showed experimentally that the developed photo-detectors can generate electric power during both the daytime and the nighttime, by either harnessing solar and thermal radiation or by emitting thermal radiation into the cold sky, including the possibility of energy harvesting from the coldness of the universe. It should be noted that both responsivity and the response time of the detector prototypes based on polycrystalline bismuth telluride active layers reported here are severely limited by the semiconductor material quality. Since the photocurrent scales linearly with the charge carrier mobility and the carrier drift time scales inversely with the mobility and the induced electric field, we expect significant improvements in both the detector responsivity and the response time by increasing the carrier mobility via use of single-crystalline materials. Epitaxially grown Bi_2Te_3 films or other single-crystal materials commonly used in IR photo-detectors, such as e.g. PbTe or PbSe, exhibit room-temperature charge carrier mobilities two-three orders of magnitude higher that the devices studied here, paving the road to corresponding improvement in the detector performance. In turn, the internal electric field scales linearly with the strain gradient and the flexoelectric coefficient of the material, offering further room for performance enhancement. Finally, the technology is not limited to Bi_2Te_3 as the active material, and offers many potential applications in night vision, wearable sensors, long-range infrared and multi-spectral LIDAR, and daytime/nighttime energy generation technologies.

Optics EXPRESS

Funding

Army Research Office (W911NF-13-D-0001); Lincoln Laboratory, Massachusetts Institute of Technology (ACC-777); H2020 Marie Skłodowska-Curie Actions (745304).

Acknowledgments

The authors thank Gang Chen, Ju Li and Nicholas Fang (MIT), Mark Polking, Melissa Smith, Cheryl Sorace-Agaskar, Mordechai Rothschild, Daniel Rippin (MIT Lincoln Laboratory), Richard M. Osgood III (CCDC Soldier Center), and Maurizio Acciarri (University of Milano Bicocca) for useful discussions.

Disclosures

The authors declare no conflicts of interest.

References

1. Q. Hong, Y. Cao, J. Xu, H. Lu, J. He, and J.-L. Sun, "Self-powered ultrafast broadband photodetector based on p–n heterojunctions of CuO/Si nanowire array," ACS Appl. Mater. Interfaces **6**(23), 20887–20894 (2014).
2. S. V. Boriskina, M. A. Green, K. Catchpole, E. Yablonovitch, M. C. Beard, Y. Okada, S. Lany, T. Gershon, A. Zakutayev, M. H. Tahersima, V. J. Sorger, M. J. Naughton, K. Kempa, M. Dagenais, Y. Yao, L. Xu, X. Sheng, N. D. Bronstein, J. A. Rogers, A. P. Alivisatos, R. G. Nuzzo, J. M. Gordon, D. M. Wu, M. D. Wisser, A. Salleo, J. Dionne, P. Bermel, J.-J. Greffet, I. Celanovic, M. Soljacic, A. Manor, C. Rotschild, A. Raman, L. Zhu, S. Fan, and G. Chen, "Roadmap on optical energy conversion," J. Opt. **18**(7), 073004 (2016).
3. S. Rühle, "Tabulated values of the Shockley–Queisser limit for single junction solar cells," Sol. Energy **130**, 139–147 (2016).
4. W. Shockley and H. J. Queisser, "Detailed balance limit of efficiency of p-n junction solar cells," J. Appl. Phys. **32**(3), 510–519 (1961).
5. J. Wang, J. Hu, P. Becla, A. M. Agarwal, and L. C. Kimerling, "Resonant-cavity-enhanced mid-infrared photodetector on a silicon platform," Opt. Express **18**(12), 12890 (2010).
6. M. Böberl, T. Fromherz, T. Schwarzl, G. Springholz, and W. Heiss, "IV–VI resonant-cavity enhanced photodetectors for the mid-infrared," Semicond. Sci. Technol. **19**(12), L115–L117 (2004).
7. B. I. Sturman and V. M. Fridkin, *The Photovoltaic and Photorefractive Effects in Noncentrosymmetric Materials* (Gordon and Breach Science Publishers, 1992).
8. V. I. Belinicher and B. I. Sturman, "The photogalvanic effect in media lacking a center of symmetry," Sov. Phys. Usp. **23**(3), 199–223 (1980).
9. A. K. Tagantsev, "Piezoelectricity and flexoelectricity in crystalline dielectrics," Phys. Rev. B **34**(8), 5883–5889 (1986).
10. J. E. Spanier, V. M. Fridkin, A. M. Rappe, A. R. Akbashev, A. Polemi, Y. Qi, Z. Gu, S. M. Young, C. J. Hawley, D. Imbrenda, G. Xiao, A. L. Bennett-Jackson, and C. L. Johnson, "Power conversion efficiency exceeding the Shockley–Queisser limit in a ferroelectric insulator," Nat. Photonics **10**(9), 611–616 (2016).
11. P. Zubko, G. Catalan, and A. K. Tagantsev, "Flexoelectric effect in solids," Annu. Rev. Mater. Res. **43**(1), 387–421 (2013).
12. L. E. Cross, "Flexoelectric effects: Charge separation in insulating solids subjected to elastic strain gradients," J. Mater. Sci. **41**(1), 53–63 (2006).
13. J. Narvaez, F. Vasquez-Sancho, and G. Catalan, "Enhanced flexoelectric-like response in oxide semiconductors," Nature **538**(7624), 219–221 (2016).
14. H. Han, D. Kim, K. Chu, J. Park, S. Y. Nam, S. Heo, C.-H. Yang, and H. M. Jang, "Enhanced switchable ferroelectric photovoltaic effects in hexagonal ferrite thin films via strain engineering," ACS Appl. Mater. Interfaces **10**(2), 1846–1853 (2018).
15. K. F. Wang and B. L. Wang, "Non-linear flexoelectricity in energy harvesting," Int. J. Eng. Sci. **116**, 88–103 (2017).
16. X. Jiang, W. Huang, and S. Zhang, "Flexoelectric nano-generator: Materials, structures and devices," Nano Energy **2**(6), 1079–1092 (2013).
17. T. Kim, W. Huang, S. Huang, and X. Jiang, "Thermal gradient induced flexoelectric effects in bulk $Ba_{0.67}Sr_{0.33}TiO_3$," Appl. Phys. Lett. **108**(19), 192902 (2016).
18. Y. Liu, J. Chen, H. Deng, G. Hu, D. Zhu, and N. Dai, "Anomalous thermoelectricity in strained Bi_2Te_3 films," Sci. Rep. **6**(1), 1–7 (2016).
19. M.-M. Yang, D. J. Kim, and M. Alexe, "Flexo-photovoltaic effect," Science **360**(6391), 904–907 (2018).
20. R. Strandberg, "Theoretical efficiency limits for thermoradiative energy conversion," J. Appl. Phys. **117**(5), 055105 (2015).

Optics EXPRESS

21. W.-C. Hsu, J. K. Tong, B. Liao, Y. Huang, S. V. Boriskina, and G. Chen, "Entropic and near-field improvements of thermoradiative cells," Sci. Rep. **6**(1), 34837 (2016).
22. P. Santhanam and S. Fan, "Thermal-to-electrical energy conversion by diodes under negative illumination," Phys. Rev. B **93**(16), 161410 (2016).
23. T. Inamoto and M. Takashiri, "Experimental and first-principles study of the electronic transport properties of strained Bi2Te3 thin films on a flexible substrate," J. Appl. Phys. **120**(12), 125105 (2016).
24. A. K. Tagantsev and A. S. Yurkov, "Flexoelectric effect in finite samples," J. Appl. Phys. **112**(4), 044103 (2012).
25. M. Stengel, "Microscopic response to inhomogeneous deformations in curvilinear coordinates," Nat. Commun. **4**(1), 2693 (2013).
26. M. Stengel, "Surface control of flexoelectricity," Phys. Rev. B **90**(20), 201112 (2014).
27. J. Tauc and M. Závětová, "Photo-piezoelectric effect in semiconductors," Czech. J. Phys. **9**(5), 572–577 (1959).
28. C. A. Klein and R. P. Miller, "Strains and stresses in multilayered elastic structures: The case of chemically vapor-deposited ZnS/ZnSe laminates," J. Appl. Phys. **87**(5), 2265–2272 (2000).
29. X. Liu, T. Zhu, H. Wang, L. Hu, H. Xie, G. Jiang, G. J. Snyder, and X. Zhao, "Low electron scattering potentials in high performance $Mg_2Si_{0.45}Sn_{0.55}$ based thermoelectric solid solutions with band convergence," Adv. Energy Mater. **3**(9), 1238–1244 (2013).
30. I. Olivares, J. Parra, A. Brimont, and P. Sanchis, "Enhancing Pockels effect in strained silicon waveguides," Opt. Express **27**(19), 26882–26892 (2019).
31. M. Cazzanelli, F. Bianco, E. Borga, G. Pucker, M. Ghulinyan, E. Degoli, E. Luppi, V. Véniard, S. Ossicini, D. Modotto, S. Wabnitz, R. Pierobon, and L. Pavesi, "Second-harmonic generation in silicon waveguides strained by silicon nitride," Nat. Mater. **11**(2), 148–154 (2012).
32. B. Mallampati, S. V. Nair, H. E. Ruda, and U. Philipose, "Role of surface in high photoconductive gain measured in ZnO nanowire-based photodetector," J. Nanopart. Res. **17**(4), 176 (2015).
33. W. Tian, Y. Wang, L. Chen, and L. Li, "Self-Powered Nanoscale Photodetectors," Small **13**(45), 1701848 (2017).
34. A. Lamminpää, M. Noorma, T. Hyyppä, F. Manoocheri, P. Kärhä, and E. Ikonen, "Characterization of germanium photodiodes and trap detector," Meas. Sci. Technol. **17**(4), 908–912 (2006).
35. C. L. Tan and H. Mohseni, "Emerging technologies for high performance infrared detectors," Nanophotonics **7**(1), 169–197 (2018).
36. W. Lei, J. Antoszewski, and L. Faraone, "Progress, challenges, and opportunities for HgCdTe infrared materials and detectors," Appl. Phys. Rev. **2**(4), 041303 (2015).
37. I. T. Witting, T. C. Chasapis, F. Ricci, M. Peters, N. A. Heinz, G. Hautier, and G. J. Snyder, "The thermoelectric properties of bismuth telluride," Adv. Electron. Mater. **5**(6), 1800904 (2019).
38. S. V. Boriskina, J. K. Tong, W.-C. Hsu, B. Liao, Y. Huang, V. Chiloyan, and G. Chen, "Heat meets light on the nanoscale," Nanophotonics **5**(1), 134–160 (2016).
39. P. Scherrer, "Bestimmung der inneren Struktur und der Größe von Kolloidteilchen mittels Röntgenstrahlen BT - Kolloidchemie Ein Lehrbuch," in R. Zsigmondy, ed. (Springer, Berlin Heidelberg, 387–409 (1912).
40. J. I. Langford and A. J. C. Wilson, "Scherrer after sixty years: A survey and some new results in the determination of crystallite size," J. Appl. Crystallogr. **11**(2), 102–113 (1978).
41. M. M. Rashad, A. El-Dissouky, H. M. Soliman, A. M. Elseman, H. M. Refaat, and A. Ebrahim, "Structure evaluation of bismuth telluride (Bi_2Te_3) nanoparticles with enhanced Seebeck coefficient and low thermal conductivity," Mater. Res. Innov. **22**(6), 1–9 (2017).
42. P. H. Townsend, D. M. Barnett, and T. A. Brunner, "Elastic relationships in layered composite media with approximation for the case of thin films on a thick substrate," J. Appl. Phys. **62**(11), 4438–4444 (1987).
43. Z. Suo, E. Y. Ma, H. Gleskova, and S. Wagner, "Mechanics of rollable and foldable film-on-foil electronics," Appl. Phys. Lett. **74**(8), 1177–1179 (1999).
44. G. M. Guttmann and Y. Gelbstein, "Mechanical properties of thermoelectric materials for practical applications," in *Bringing Thermoelectricity into Reality* (InTech, 2018).
45. J. S. Kim, K. W. Paik, and S. H. Oh, "The multilayer-modified Stoney's formula for laminated polymer composites on a silicon substrate," J. Appl. Phys. **86**(10), 5474–5479 (1999).